Energy Science & Engineering

ORIGINAL ARTICLE OPEN ACCESS

Single Step and Solution Process Fabrication of Mesoporous ZnOS Thin Film as an Effective Electron Transport Layer for the Cs-Based Halide Double PSCs

Md. Jakir Hossen[1,2] | Md. Bulu Rahman[3] | M. Shahinuzzaman[4,5] | Md. Helal Miah[3] | Noor-E. Ashrafi[3] | Abdur Rahim[4] | Suhana Mohd Said[1] | S. F. W. M. Hatta[1,6] | Mohammad Aminul Islam[1,6,7]

[1]Department of Electrical Engineering, Faculty of Engineering, Universiti Malaya, Kualalumpur, Malaysia | [2]Department of Physics, Hajee Mohammad Danesh Science and Technology University, Dinajpur, Bangladesh | [3]Department of Physics, Gopalganj Science and Technology University, Gopalganj, Bangladesh | [4]Institute of Energy Research and Development, Bangladesh Council of Scientific and Industrial Research (BCSIR), Dhaka, Bangladesh | [5]Department of Electrical and Electronic Engineering, Uttara University, Dhaka, Bangladesh | [6]Centre of Printable Electronics, Universiti Malaya, Jalan Universiti, Kuala Lumpur, Selangor, Malaysia | [7]Miyan Research Institute, International University of Business Agriculture and Technology (IUBAT), Dhaka, Bangladesh

Correspondence: Md. Jakir Hossen (jakir@tch.hstu.ac.bd) | Mohammad Aminul Islam (aminul.islam@um.edu.my)

Received: 20 April 2025 | **Revised:** 6 September 2025 | **Accepted:** 9 September 2025

Funding: This study was supported by the Malaysian Ministry of Higher Education through FRGS grant FRGS/1/2020/TK0/UM/02/33 and Malaysian International Scholarship (MIS) 2022.

Keywords: device modeling | halide double PSCs | SCAPS-1D | single step | ZnOS

ABSTRACT

In this study, the ZnOS thin films have been fabricated by the spin coating technique for applying as an effective electron transport layer (ETL) for halide double perovskite solar cells (PSCs). The impact of the number of coatings and/or thickness variations on ZnOS thin films' properties has been analyzed in terms of surface morphology, crystal structure, elemental, and optoelectronic characteristics, and has been found to have a substantial impact on the properties of prepared thin films. For better understanding, an undoped ZnO thin film has also been analyzed alongside the ZnOS thin films. Also, the performance variation of halide double PSCs has been investigated utilizing ZnOS as an effective ETL by means of a solar cell capacitance simulator one-dimensional software. The highest power conversion efficiency (PCE) with the configuration of FTO/ZnOS/$Cs_2AgBi_{0.75}Sb_{0.25}Br_6$/$Cu_xO$/Au of 16.21% was obtained for single-coated ZnOS thin films. The result implies that ZnOS can more efficiently extract the charge carriers from the absorber layer of PSCs than pure ZnO. We anticipate that the findings of this study will lead to fresh insights into the practical applications of ZnOS as the optimum ETL for halide double PSCs.

1 | Introduction

Perovskite solar cells (PSCs) exhibit 26.95% PCE recently, which is near to the commercially available Si-based solar cell [1]. However, for one of the highest performances for ZnO-quantum dot-based PSCs with a PCE of 21.74% [2]. They are mainly composed of different components, including the ETL, the hole transport layer (HTL), and the absorber layer (Abs). A photovoltaic device's performance is determined by its perovskite layer, ETL, HTL, and interface properties [3–5]. These interfaces are also responsible for the trapping of charge carriers and recombination, which causes low photo conversion efficiency. This problem can be resolved by adapting compatible ETL [6], HTL [7], along with appropriate perovskite material, leading to decreases in the defect density and increases in the efficiency and stability of the PSCs [8]. To transmit electrons and inhibit holes inside the ETL, the trans-electrode typically needs to be transparent to visible light and also needs to have a wide

bandgap, strong electron mobility, and an acceptable conduction band offset between ETL/Abs [9]. ZnOS is a nontoxic, environment-friendly ETL that can be easily produced by solution-based techniques at very low temperatures [10]. It has a tunable bandgap (2.6–3.8 eV) compared with the 2.42 eV of CdS, and with an n-type conductivity which allows it to absorb photons with high efficiency [11]. ZnOS also shows tremendous surface passivation, which increases open circuit voltage (V_{oc}) as well as PCE of the PSCs. Due to their enormous size and the difference in electronegativity between the two anions, partial substitution of S^{2-} ions with O^{2-} ions in ZnO may result in notable modifications to the electrical and optical properties [12, 13]. All these promising properties of the ZnOS ETL make it a suitable candidate for use as an ETL in a solar cell, which reduces interfacial loss and enhances device performance with less hysteresis.

On the other hand, despite the similar hexagonal wurtzite structures of ZnO and ZnS, the solubility limitations of sulfur in ZnO and oxygen in ZnS at typical deposition temperatures make it difficult to create the $ZnO_{1-x}S_x$ alloy [14]. Higher temperature synthesis of the ETL layer can disrupt adjacent layers in heterostructures, reducing overall device efficiency [15]. Furthermore, producing $ZnO_{0.5}S_{0.5}$ in a single phase is challenging, and it is difficult to investigate its physical properties [16]. Techniques like atomic layer deposition (ALD) [17], chemical bath deposition (CBD) [18], and pulsed laser deposition [19] have been used to synthesize ZnOS, but these methods are often complex and time-consuming [15]. CBD, in particular, offers an affordable and adjustable method for ZnOS thin film fabrication. However, in the $ZnO_{1-x}S_x$ ETL, a significant discrepancy in the electronegativities of sulfur and oxygen results in modifications to the electron potential as well as the lattice potential, which ultimately causes bandgap bowing [20]. It is difficult to produce $ZnO_{1-x}S_x$ alloys over the whole composition range because the wider the miscibility gap [21], the larger the bending [22]. For these reasons, knowledge of $ZnO_{1-x}S_x$ basic characteristics is crucial for material science as well as for its potential applications [23]. In this study, instead of multistep approaches, we are proposing a low-cost, easily fabricable, solution process (wet chemical) technique. The ZnOS thin films can fabricate at room temperature, and can be tuned chemically to synthesize ZnOS material with the right complexing agent. Here, right solvent and its concentration have been optimized among Chlorbenzene, *n*-butanol, isopropyl alchohol (IPA), chloroform, ethanol solvents. We concentrated on how the number of thin film coatings affected the structural, optical, and electrical properties as a result of recrystallization. Subsequently, a theoretical simulation has been performed employing solar cell capacitance simulator (SCAPS) one-dimensional (1D) software by using experimental data of this ZnOS and other data from previous literature to find the impact of the number of coatings and/or thickness variations of ZnOS thin films. The ZnO thin film has also been analyzed alongside to verify its performance as an ETL layer of a double halide $Cs_2AgBi_{0.75}Sb_{0.25}Br_6$ PSCs. Here, transparent Cu_xO has been chosen for the HTL recently because of its high charge carrier (hole) mobility, low electron affinity, ideal direct narrow bandgap semiconductor (e.g., 2.1–2.2 eV) regarding the device layers, and most significantly, its inorganic nature, which results in low degradability [24]. Particularly, $Cs_2AgBi_{1-x}Sb_xBr_6$ lead-free double-perovskite (HDP) is yet to less explored and showed potential photovoltaic properties for solar cell application [25]. For instance, Liu et al. [26] reported PCE of 0.25% for HDP solar cells with the structure of FTO/dense-TiO_2/*m*-TiO_2/$Cs_2AgBi_{0.75}Sb_{0.25}Br_6$/Spiro-MeOTAD/Au, and Kumar et al. [27] reported PCE of 0.09% or HDP solar cells with the structure of FTO/NiO_x/$Cs_2AgBi_{0.6}Sb_{0.4}Br_6$/PCBM/Ag. The numerical analysis performed in this study revealed that the PCE of the HDP solar cell might exceed 16%, which is achievable by using appropriate ETL and HTL as well as optimizing the perovskite layer.

2 | Experimental Methods

Zinc acetate dihydrate ($Zn(CH_3COO)_2{\cdot}2H_2O$) 99.99%, sodium hydroxide (NaOH), sodium thiosulphate pentahydrate ($Na_2S_2O_3{\cdot}5H_2O$), acetic acid (CH_3COOH), and ethanol (CH_3CH_2OH) were purchased from Merck, Germany. *N*-butanol($C_4H_{10}O$) was purchased from Smart Lab, Indonesia. Isopropyl alcohol ($CH_3CH_2CH_2OH$) and acetonitrile (CH_3CN) were from Sigma-Aldrich, USA. Without additional purification, every chemical and reagent were employed.

A 10.975-gm zinc acetate dihydrate was mixed with 50 mL deionsed (DI) water to make it a 1-M solution. Then, 10 mL NaOH (1 M) was mixed with the solution dropwise. A 3.902-gm sodium thiosulphate pentahydrate ($Na_2S_2O_3{\cdot}5H_2O$) was mixed with 50 mL DI water. After that solution was added to the precursor for doping sulfur ion and stirred with a magnetic stirrer for about 120 min at 60°C. Precipitate was filtered, then washed and mixed with 170 mL of acetic acid to dissolve. A rotary evaporator was used to separate acetic acid, and ethanol was added to collect the samples from the rotary evaporator. Then the sample was kept inside an oven at 105°C for proper drying. Then, dried ZnOS nanoparticles were ground using a ball-milling process before use.

To make the precursor solution, first, 2 mL chloroform, 0.5 mL *n*-butanol, and 2.5 mL chlorobenzene were added with 0.15 gm ZnOS powder. But a star-like formation on the film surface was observed. A 5-mL HNO_3 mixed with 0.15 gm ZnOS powder was added together, and after 15 min sonication applied to dissolve the powder. After spin coating on a glass substrate, the observed film was not smooth due to not properly dissolve the ZnOS powder. Then, to optimize the right solvents for smooth film morphology, the other solvents like IPA, ethanol, and *n*-butanol were applied and varied their concentration with the amount of ZnOS powder (0.075 gm) was kept constant. Finally, a smooth film was observed for precursor solution 0.075 gm ZnOS powder mixed with 2 mL IPA, 0.5 mL ethanol, and 2.5 mL *n*-butanol at ambient environment. The fabrication of the thin film glass substrate was first cleaned with an ultrasonic bath with soap solution for 15 min, then cleaned with acetone and IPA with an ultrasonic bath for 10 min each. The glass substrate was rinsed with DI water in between every wash. A spin coater was used to fabricate the film at a speed of about 500 rotations per minute (rpm) for 10 s and then 3000 rpm for 60 s. All the films have been annealed at 110°C each time, then the next coating has been done onto the film at the same speed as the spin coater. After completing different numbers of coatings (i.e., 1, 2, and 3 times), each film was annealed at 110°C for 10 min. All this fabrication process was done in the ambient environment inside a fume hood.

For this investigation, sophisticated analytical tools such as a Fourier transform infrared (FTIR) spectrophotometer (Perkin Elmer Spectrum two, wavenumber range 8300–350 cm^{-1}) and an X-ray diffractometer (Drywell XRD-7000, CuKα [$\lambda = 1.54178$ Å] radiation) were employed. Van der Pauw variable temperature Hall effect measurement device (Ecopia HMS3000) was used to measure electrical properties, like, resistivity, carrier concentration, and carrier mobility. A UV–vis spectrometer (SPECORD 200 PLUS-223E1128F analytic, Germany) was used to examine the optical characteristics (absorbance and optical bandgap) of these produced thin films in the wavelength range of 200–800 nm. Since photon energy is equal to the optical bandgap (E_g) when $(\alpha h\nu)^2$ becomes zero, the E_g of the films can be calculated by extrapolating the $(\alpha h\nu)^2$ versus $h\nu$ curve. For field emission scanning electron microscope (FESEM) analysis, the ZnOS thin films were first gold (Au) coated (CRESINGTON SPUTTER COATTER-108, Ted Pella Inc., USA) before introducing into the FESEM (ZEISS Gemini SEM 500) chamber, and subsequently an accelerating voltage between 5 and 10 kV was used to determine their overall morphology. The elemental qualitative analysis was performed using energy dispersive spectroscopy (EDS) attached to FESEM. SCAPS-1D software was used to observe the solar cell performance of ZnOS as an ETL from the data experimentally mined from this study.

3 | Result and Discussion

3.1 | Structural Properties

The structural properties of ZnOS thin films as ascertained by X-ray diffraction (XRD) are displayed in Figure 1. The patterns of undoped ZnS showed a hexagonal wurtzite structure having diffraction planes at 26.49 (100), 27.46 (002), 51.57 (103), 55.19 (200), and 78.64 (114), which coincide with the value of JCPDS Card No. 36-1450. Undoped ZnO exhibited diffraction planes at 33.76 (002), 37.70 (101), 61.65 (103), and 65.57 (200), showing a typical hexagonal wurtzite structure, in line with JCPDS Card No. 36-1450's value. In other words, the XRD results showed ZnS phases, and ZnO phases present in all the ZnOS thin films.

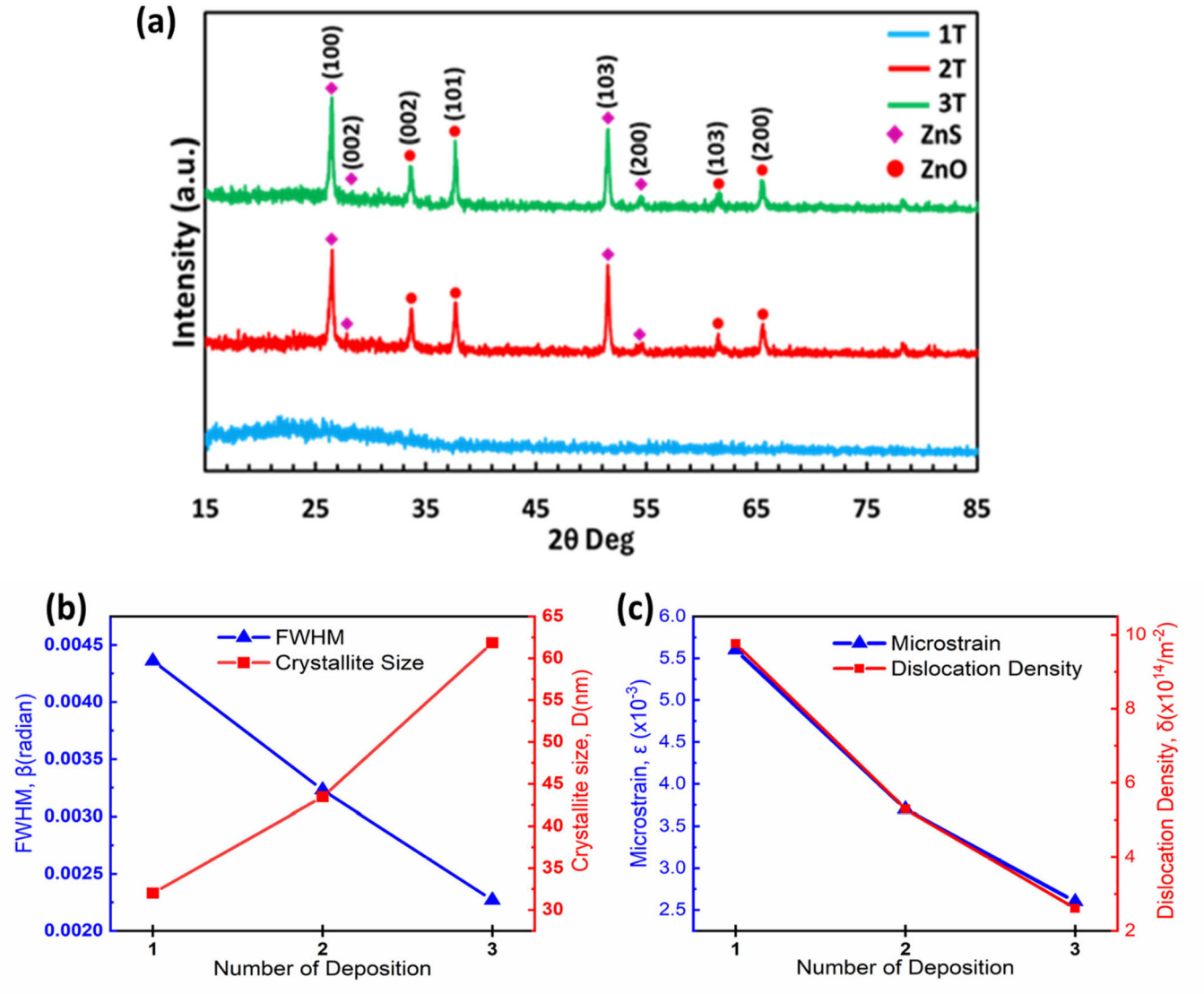

FIGURE 1 | (a) XRD pattern of ZnOS thin film ETL layer, (b) FWHM and crystallite size, and (c) microstrain and dislocation density for 1-, 2-, and 3-times coating. ETL, electron transport layer; FWHM, full-width at half-maximum; XRD, X-ray diffraction.

This implies that zinc has chemical bonds with both sulfur and oxygen. We may infer from the XRD that recrystallization of ZnOS occurred at a higher thickness, leading to a rise in effective size. Moreover, as the percentage of sulfur increases, the XRD peaks of these atoms move to larger angles due to the decrease in lattice constant caused by their smaller size.

It should be noted that the film deposited by single-time deposition was found to be an amorphous structure. The polycrystalline film observed for multiple depositions may be related to the impact of the nature of the bottom layer and/or the nature of the substrate. It should be noted that a substantial difference in the lattice parameters of the deposited material and the substrate may inhibit epitaxial development and result in reduced crystallinity [28]. Thus, single-deposited ZnOS films are found to be amorphous as the bottom layer is SiO_2 (glass). However, for the second or later layers, the bottom layer is ZnOS. The nature of the substrate plays an important role in the crystalline structure of the films.

The estimated structural properties extrapolated from the XRD are shown in Table 1. The crystallite size has been calculated using Scherrer's equation, $D = 0.9\lambda/\beta\cos\theta$. Here, D is the average crystallite size, θ represents the angle of Bragg's diffraction, λ is the X-ray wavelength (1.5406 Å for the CuKα line), and β is the full-width at half-maximum (FWHM) in radians. The computation was done using the FWHM of the main peak (100) among the peaks. ZnOS crystal sizes range from 32.01 to 61.84 nm, which increases with the increase in the number of depositions, resulting in larger grain sizes. It should be mentioned that the amorphous crystal structure observed for single-coated films around 2θ of 21.87° shows the possibility of an amorphous phase in these materials. The interplanar spacing can also be computed using Bragg's equation, $d = n\lambda/2\sin\theta$, where λ is the X-ray wavelength, n is an integer, and θ is Bragg's diffraction angle [29]. The larger spacing found at single-coated or one-time-coated film as its grain size is smaller than the other multiple times coated films. The dislocation density expresses the defects per unit volume and vacancies, which can be calculated by the relation $\delta = 1/D^2$. The inverse relation between dislocation density and crystallite size represents the large number of lattice imperfections that occur with low crystallite size, as shown in Figure 1b,c. The author found the lowest dislocation density for three-times coating, which shows better thin film morphology. The microstrain causes the XRD lines to broaden without changing the peak position. It can be calculated by $\varepsilon = \beta/4\tan\theta$. This is calculated by the crystal's interatomic distance change. The lowest microstrain observed in the case of three-times deposition, which represents the better crystallinity of the film as shown in Figure 1b,c.

3.2 | Optical Properties

For the application of a material as an ETL, lower absorbance is a good indication. Figure 2a shows the absorption spectra of the ZnOS and undoped ZnO ETL layer in the range of wavelength 300–800 nm with different numbers of coatings. The ZnOS nanoparticles with 3-times deposition showed stronger absorption peaks than those of 2-times and 1-time coating of ZnOS. Absorbance depends on the deposition potential, for example, absorbance rises as the potential for deposition rises [10]. However, undoped ZnO shows a lower absorption. To attain low absorbance in solar cells, materials used as ETL layers should have a thickness of approximately ≤ 100 nm [10]. This study completely agrees with this statement as we can see that the absorption is higher for the films of 3-times coated than 2-times and 1-time coating since the increasing thickness of ZnOS thin film. This reduction in the absorbance of lower-thickness ZnOS thin film makes it a good candidate for use as an ETL layer in PSCs [10]. This implies that more photons will be permitted to enter the cell, resulting in the production of more charge carriers. Alternatively, the reduction of the thickness for the higher transmission of the ETL/buffer layer induces a slight increase in the bandgap.

To understand the optical properties of the fabricated ZnOS, the optical bandgap has also been calculated. The bandgap (E_g) of a direct bandgap material as well as the ZnOS thin films is calculated based on the following Tauc equation [30]:

$$\alpha = A(h\upsilon - E_g)^n/h\upsilon. \quad (1)$$

In this equation, α is the absorption coefficient, $h\nu$ is the photon energy, E_g is the bandgap, and A is a proportionality constant [31]. Figure 2b shows linear fits of $(\alpha h\nu)^2$ versus $h\nu$ graph of ZnOS, giving clear optical bandgaps of 2.76, 2.72, and 2.68 eV, for 1-, 2-, and 3-times coating, respectively. In the case of undoped ZnO, it was 3.16 eV, as shown in the inset of Figure 2b. It was found that the energy gap decreased with the increase in the number of coatings. Moreover, the fabricated ZnOS films, however, exhibit various absorption properties at higher wavelength regions. Particularly, transitions between band tail states below the bandgap are liable for the effective absorption features observed in the visible area. An elevated density of band tail states can form inside the bandgap as a film's degree of disorder grows, which refers to as Urbach energy tails. The energy controlled by structural disorder, imperfection, and passivation at the surface is known as Urbach energy, which appears under the conduction band edge and over the valence band edge. In 1953, Franz Urbach of the Kodak Company

TABLE 1 | Calculated crystal structural information of 1-, 2-, and 3-times coated ZnOS thin film at 100°C annealing for about 10 min.

Number of depositions	*hkl* plane	2θ (°)	FWHM, β (radian)	Crystallite size, D (nm)	d-Spacing (Å)	Microstrain, ε	Dislocation density, δ (10^{14} m^{-2})
1-Time	(100)	21.87	0.00436	32.009	4.06	0.0056	9.76
2-Times	(100)	24.49	0.00323	43.459	3.63	0.0037	5.29
3-Times	(100)	24.46	0.00227	61.842	3.63	0.0026	2.61

Abbreviation: FWHM, full-width at half-maximum.

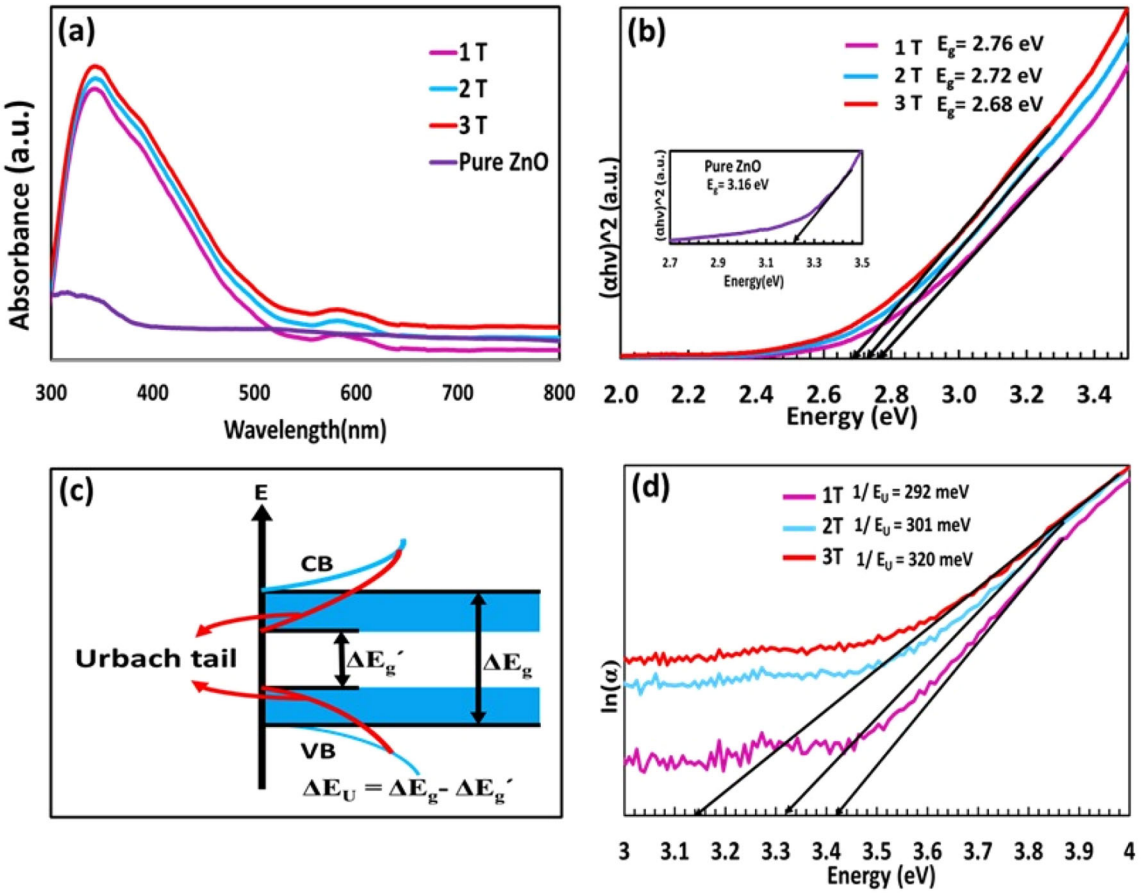

FIGURE 2 | (a) Absorbance of ZnOS ETL layer with 1-, 2-, and 3-times coating on a glass substrate, (b) Tauc plot for a bandgap of ZnOS ETL layer with 1-, 2-, and 3-times coating on glass substrate, (c) schematic diagram of Urbach energy evolution, and (d) ln α versus $h\nu$ for 1-, 2-, and 3-times coating. ETL, electron transport layer.

conducted a thorough evaluation of this characteristic in crystals using silver bromide. The Urbach relation describes the optical transition between band tail states as follows: E_U is the Urbach energy, and α_0 is a constant [30–32].

$$\alpha = \alpha_o e^{h\upsilon/E_u}. \quad (2)$$

The behavior of the absorption spectrum is exponentially decreasing below the band edge transition energy, suggesting Urbach tail features near the absorption edge [33]. Figure 2c shows a schematic diagram of the Urbach energy evolution onset. The band edge steepness of absorption starts, and, consequently, the density of the states' breadth is quantified by the Urbach energy.

$$\alpha = \alpha_o e^{(E_g/KT)\beta}. \quad (3)$$

where β is a so-called steepness parameter that characterizes the absorption edge's broadening as a result of the electron–phonon or exciton–phonon interaction. When the edge's width is connected to Equation (2) slope, the parameter β can be determined as

$$\beta = KT/E_u. \quad (4)$$

Smaller Urbach energy is indicated by a sharper absorption onset. The Urbach energy also depends on the temperature, which varies from a few to MeV, and is inversely proportional to its bandgap energy (E_g). Since Urbach energy can be determined from the slope, a linear plot of ln α versus $h\nu$ is expected [34]. The ZnOS thin film variance for various preparation procedures is plotted against $h\nu$ in the Figure 2c graph. E_U was computed using the linear component of these curves' reciprocal gradient, and it is displayed in Figure 2d.

Computed values are provided in Table 2. Here, lower E_U values 292–320 eV were observed compared with the reference value 320–540 MeV, which was fabricated by the ALD technique by Yu et al., 2018. The higher the Urbach energy values, the larger the lattice disorder present in the sample. This tends to low device stability and defect tolerance. Where the E_U increases with the increase of the number of coatings, and steepness β decreases with the increase of the number of coatings. Therefore, the E_U provides details regarding the thermal disorder or the degree of phonon state occupancy in crystals [30]. Nevertheless, E_U can also be modeled as an Einstein oscillator by considering Skettrup's theory. This allows for the calculation of the sample's structural and thermal disorder [32]. The results of this investigation are consistent with the general observation that the E_U values fluctuate inversely with the optical bandgap

TABLE 2 | E_g, β, this study E_U, and the reference value of the ZnOS thin film @ $T = 110°C$.

Sample variation	Bandgap E_g (eV)	β (10^{-3})	This study E_U (MeV)	Reference E_U (MeV) [12]
1-Time coating	2.76	88.61	292	540
2-Times coating	2.72	85.96	301	210
3-Times coating	2.68	80.85	320	320

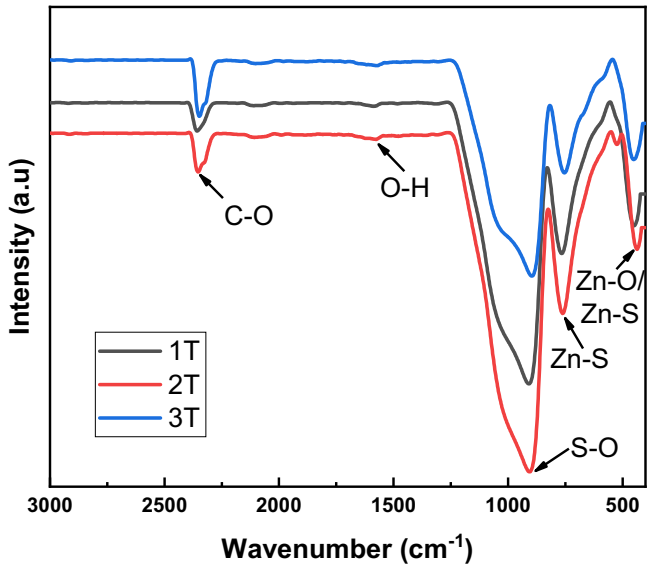

FIGURE 3 | Fourier transform infrared image of 1-, 2-, and 3-times coating of ZnOS thin film.

of thin films. The information in Table 2 clearly indicates that the larger the E_U, the narrower the bandgap (E_g).

3.3 | Functional Group Analysis

The FTIR spectra of ZnOS thin films coated 1, 2, and 3 times, as shown in Figure 3, confirm the presence of several key functional groups related to ZnOS formation and associated bonding interactions. In the low wavenumber region, strong absorption bands are observed around 460 cm^{-1}, characteristic of Zn—O/Zn—S stretching vibrations. These peaks confirm the formation of ZnO and ZnS in the Zn(O, S) lattice [35].

The ZnO peak intensity increased with increasing the coating cycle, indicating enhanced film densification and more developed oxygen bonding with thicker layers. The peaks at 773 cm^{-1} have been attributed to the vibration of Zn—S bending bonds [36]. Broad peaks around 930 cm^{-1} are likely associated with the symmetric stretching vibrations of S—O bonds [37] and/or attributed to the resonance interaction between vibrational modes of sulfide ions of the crystal [35]. As a result of the complex structure of capping agent sources, the peaks tend to broaden and combine with shoulders for different functional groups. These bands weaken slightly in the 3T sample, indicating better film uniformity and fewer sulfur residues. The absorption band at 1630 cm^{-1} occurs because of O—H bending [38]. A sharp peak around ~2370 cm^{-1} indicates C—O stretching. This stretching could be arisen from the background interference of atmospheric CO_2 [39, 40]. Overall, the FTIR analysis confirms the chemical formation of ZnOS and provides insight into its surface functionalization, with each coating cycle maintaining consistent vibrational features. Table 3 shows the respective functional group with relevant references and the wavenumber observed in this study.

3.4 | Surface Morphology and Elemental Analysis

Mesoporous morphology of ZnOS layer observed in the FESEM image in Figure 4a–c. A benefit of mesoporous scaffolds is that because the nanocrystalline oxide permits the bulk Abs layer, less transport length is needed for photogenerated electrons from the Abs to reach the ETL layer [41]. According to reports, recombination loss caused by structural instabilities at grain boundaries can result in defect states that deteriorate perovskite films [42–44]. Hence, recombination loss resulting from structural instabilities at grain boundaries has been shown to produce defect states that degrade perovskite films. The dense nanocrystal could be seen in Figure 4, which may have happened due to recrystallization between Zn^{2+} and S^{2-} ions in the ZnOS matrix. We can infer that the creation of dense nanocrystal may oppose ZnOS to decompose and increase the film stability [13]. The film's elemental composition was verified by EDS mapping as shown in Figure 4d. The elemental ratio of the one-time coated film is Zn (10.95%), O (46.04%), S (1.24%), and Na (12.76%). Particularly, Si and C are found to be in every sample in very small amounts. However, the Na and Zn peaks are positioned so closely that they are likely to overlap. The elemental ratios of other films are shown (only Zn, S, and O) in Table 4. Recent studies show that alkali-metal ions (like Li^+ and Na^+) can penetrate ZnO and ZnS nanocrystals, becoming trapped in shallow subsurface layers and causing surface/interface defects, contrary to the assumption that they remain in solution [38, 45]. Such contamination is significant because the physicochemical properties of ZnO nanocrystals are highly sensitive to intrinsic defects and impurities [45]; however, this phenomenon is rarely discussed in the previous literature. Addressing this issue is crucial for sol–gel derived materials, with wet-organometallic strategies offering effective routes for producing high-quality, alkali-metal-free ZnO nanocrystals. We intend to investigate it further and publish the results elsewhere.

3.5 | Electrical Properties

Carrier concentration, mobility, resistivity, and corresponding to the elemental ratios of ZnOS thin films are shown in Table 4. It should be noticed that the electrical properties of ZnOS film strongly depend on carrier concentrations from S^{2-} on Zn^{2+} ions, S and Zn interstitial atoms, and oxygen vacancies. In ZnO and ZnOS, resistivity is predominantly governed by the carrier concentration (n) and Hall mobility (μ), following the relationship given in Equation (5):

TABLE 3 | Different functional groups and their wavenumber with reference value.

Band position (cm^{-1})				
1T	**2T**	**3T**	**Functional group/assignment**	**Reference**
462.72	464.61	470.22	Zn–O/Zn–S	[35]
773.08	774.15	773.15	Zn–S	[36]
928.91	930.34	931.51	S–O	[35]
1630.53	1630.79	1631.6	O–H bending	[38]
2371.11	2371.98	2372.31	C–O	[39, 40]

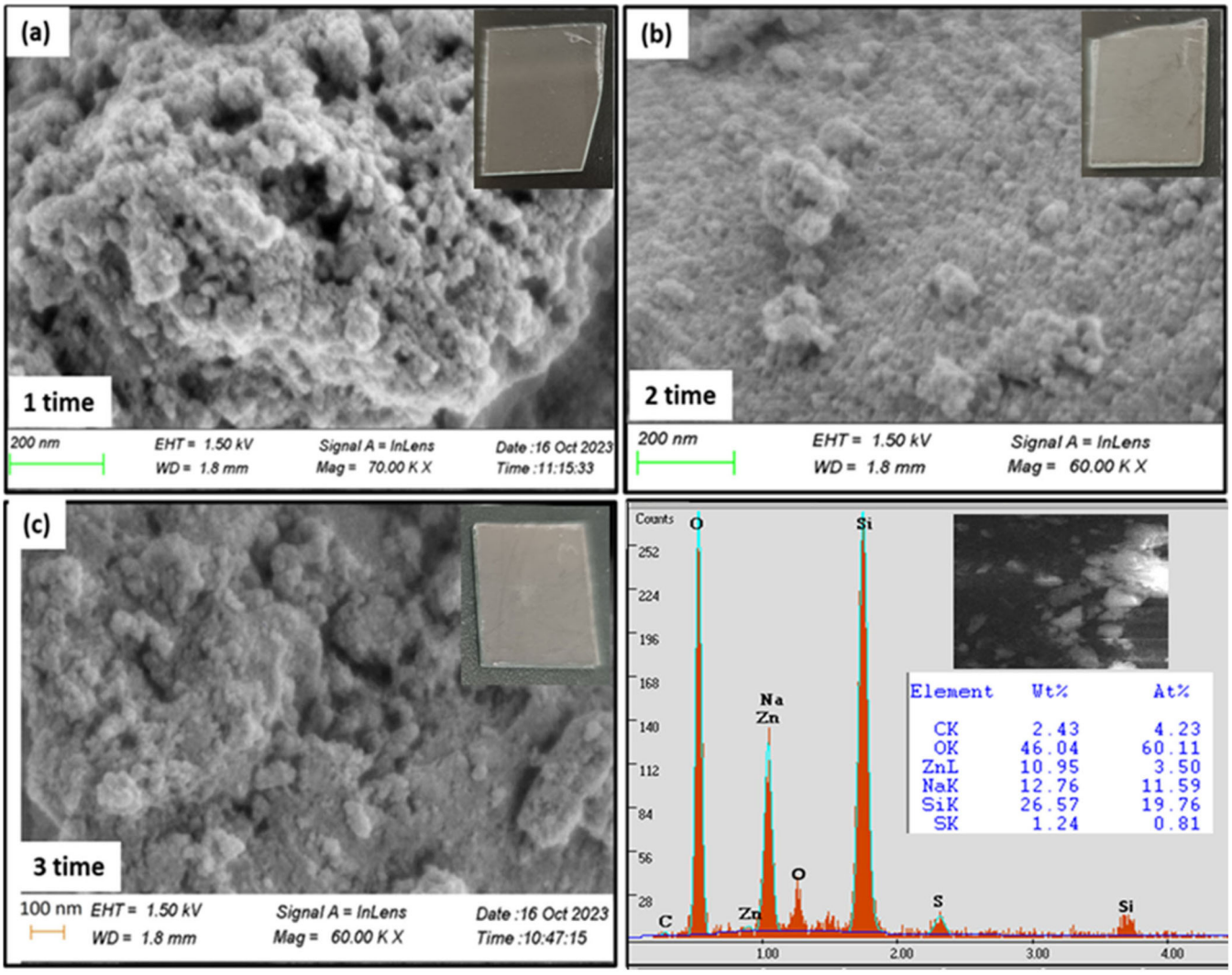

FIGURE 4 | (a–c) 1-, 2-, and 3-times coating FESEM image of ZnOS thin film, and (d) EDS for one-time coated thin film, (inset 1-, 2-, and 3-times coated film). EDS, energy dispersive spectroscopy; FESEM, field emission scanning electron microscope.

TABLE 4 | Carrier concentration, carrier mobility, and resistivity of ZnOS thin film with various thicknesses.

Number of depositions	At (%)			Concentration (n) ($\times 10^{16}$) cm^{-3}	Mobility (μ) ($cm^2 V^{-1} s^{-1}$)	Resistivity (ρ) ($\times 10^{-4}\,\Omega\,cm$)
	Zn	**S**	**O**			
Undoped ZnO	79.2	—	23.0	13.08	10.13	8.94
1-Time coating	10.95	1.24	46.04	5.91	27.50	4.18
2-Times coating	49.5	9.8	25.1	1.60	42.20	3.63
3-Times coating	61.7	20.7	9.8	6.03	16.60	3.00

$$\rho = \frac{1}{n\mu e}. \quad (5)$$

In this expression, e represents the elementary charge constant (1.602×10^{-19} C), n denotes the free charge carrier density, and μ corresponds to the carrier mobility obtained from Hall effect measurements. This relationship demonstrates that ZnO's resistivity decreases with higher carrier concentrations and greater charge carrier mobility. The intrinsic ZnO films exposed electrical resistivity of the order of $1.97 \times 10^{2}\ \Omega$ cm. After doping with S ion, it reduces to $4.18 \times 10^{-4}\ \Omega$ cm for one-time coatings and slightly decreases further with the number of coatings. This is due to an increase in the carrier concentration with the number of coatings. For three-times coating, carrier concentration rises to a maximum value of $6.03 \times 10^{16}\ \text{cm}^{-3}$. The variation of carrier mobility may be related to the increase of lattice defect induced by the S and O atoms in the film, as seen in Table 4.

The carrier mobility in doped metal oxide semiconductors can be analyzed using Matthiessen's rule, which accounts for multiple scattering mechanisms: can be described by the following mathematical expression:

$$\frac{1}{\mu} = \frac{1}{\mu_i} + \frac{1}{\mu_g} + \frac{1}{\mu_l}. \quad (6)$$

Here, μ_i represents ionized impurity scattering, μ_g denotes grain boundary scattering, and μ_l corresponds to lattice phonon scattering (thermal vibration effects). In S-doped ZnO thin films, ionized impurity scattering becomes more significant at higher doping concentrations, imposing a major limitation on mobility. Meanwhile, phonon scattering (μ_i) is typically negligible except at higher temperatures. Consequently, the primary mobility-restricting factors are impurity scattering and grain boundary effects. For sulfur-doped ZnO (ZnOS) films with identical doping levels, impurity scattering remains relatively consistent due to their uniform chemical composition, leaving grain boundary scattering as the dominant variable influencing mobility differences. Hall mobility is significantly affected by grain boundary scattering, which plays a dominant role in electron transport. S-doped ZnOS films exhibit enhanced crystallinity, which suppresses grain boundary scattering and consequently increases Hall mobility. The highest carrier mobility is observed for the film prepared by two-times coating. The minimum resistivity value obtained in this study was $3 \times 10^{-4}\ \Omega$ cm for three-times coatings, which can be further improved with preheating and ensuring a controlled atmosphere throughout annealing. In the case of undoped ZnO, the carrier concentration is about $13.08\ \text{cm}^{-3}$, resistivity $8.94 \times 10^{-4}\ \Omega$ cm, and bandgap 3.2 eV, which is higher than that of ZnOS. However, the mobility of ZnO ($10.13\ \text{cm}^2\ \text{V}^{-1}\ \text{s}^{-1}$) was observed less than that of ZnOS ($42.20\ \text{cm}^2\ \text{V}^{-1}\ \text{s}^{-1}$) thin film, which makes ZnOS better ETL than undoped ZnO. The obtained mobility performance is higher than that of sulfur-treated ZnO ($16.27\ \text{cm}^2\ \text{V}^{-1}\ \text{s}^{-1}$) as reported in references. It is obvious that S doping increases the mobility and decreases its resistivity linearly. However, mobility reduces after two times coating. This may be the increases in the S concentration in the samples, which impurity scattering becomes more significant at higher doping concentrations. For each deposition technique, three samples were measured, and the average values were presented in Table 4. Additionally, Figure 5 illustrates these results with error bars included for further clarification.

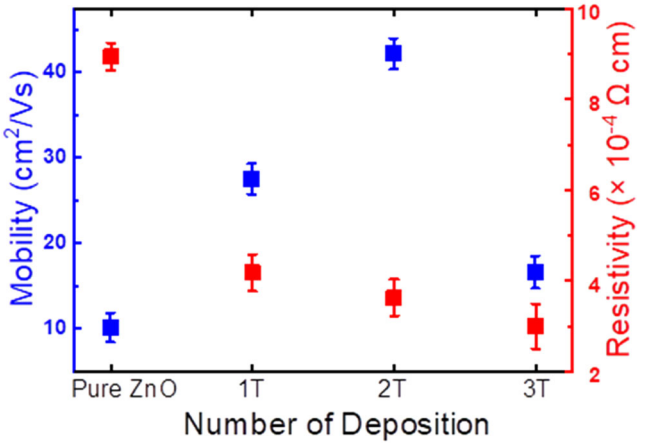

FIGURE 5 | Mobility and resistivity of pure ZnO and S-doped ZnO with different numbers of depositions.

4 | Device Simulation and Performance Evaluation

The SCAPS-1D software has been used to analyze and compare the photovoltaic performances between undoped (ZnO) and sulfur-doped (ZnOS) as an ETL in the FTO/ZnOS/$Cs_2AgBi_{0.75}Sb_{0.25}Br_6$/$Cu_2O$/Au double PSC structure using experimental data from this study. SCAPS-1D is a highly efficient and user-friendly solar cell simulator, outperforming other tools, like, COMSOL, SILVCO, AMPS, and so forth [46–48]. It can simulate up to seven various layers in a heterostructure system and operate under various ambient conditions, consistently aligning well with experimental results [49–51]. The following initial parameters from Table 5 have been used to simulate this device structure. Figure 6 and Table 6 show the results found from the numerical simulation utilizing the inverted planner halide double PSC structure of Glass/FTO/Cu_xO/$Cs_2AgBi_{1-x}Sb_xBr_6$/ZnOS/Au. It could be seen that all the performance parameters are increased for one-time coatings than the undoped ZnO, which reduced further the increase in the number of depositions. The direct correlation between fill factor (FF) and the charge extraction and transport that took place in PSC is widely recognized. Moreover, the mobility of the carrier, the film's shape, and the solar cell's interfacial and bulk charge recombination rates all affect the extraction and movement of charges. The carrier recombination, which may be impacted by interface states and defects in the individual active layers, determines J_{sc} in the conventional n–i–p semiconductor model, while V_{oc} depends on the splitting of the quasi-Fermi energy levels of the electron and hole in the entire system. Additionally, J_{sc} is influenced by the perovskite materials' spectrum response. Therefore, the charge transport layer and energy distribution of the perovskite thin films have a major impact on the PSC's performance [57, 58].

The light J–V curve also shown in Figure 6a inset, a lower current–voltage combination occurs for undoped ZnO, and the best performance is shown in the case of one-time coatings, that is, at lower thickness. As the thickness increases the performance

TABLE 5 | The initial physical parameters of ETL, absorber layer, and HTL.

Parameters	FTO	ZnO	ZnOS	$Cs_2AgBi_{1-x}Sb_xBr_6$	Cu_xO
Thickness t (nm)	500	70	70	400	350
Bandgap E_g (eV)	3.5	3.3	2.83 (varied)	1.8	2.17
Electron affinity χ (eV)	4.00	4.00	3.6	3.58	3.2
Dielectric permittivity ε_r	9.00	9.0	9.0	6.5	7.1
CB effective density of states N_c (cm^{-3})	2.2×10^{18}	3.7×10^{18}	2.2×10^{18}	2.2×10^{18}	2.02×10^{17}
VB effective density of states N_v (cm^{-3})	1.8×10^{19}	1.8×10^{19}	1.8×10^{18}	1.8×10^{19}	1.10×10^{19}
Electron thermal velocity V_e ($cm\,s^{-1}$)	1×10^{7}	1×10^{7}	1×10^{7}	1×10^{7}	1×10^{7}
Hole thermal velocity V_h ($cm\,s^{-1}$)	1×10^{7}	1×10^{7}	1×10^{7}	1×10^{7}	1×10^{7}
Electron mobility μ_e ($cm^2\,V^{-1}\,s^{-1}$)	20	100	100 (varied)	2	200
Hole mobility μ_h ($cm^2\,V^{-1}\,s^{-1}$)	10	25	25.0	2	80
Shallow uniform acceptor density N_A (cm^{-3})	0	0	0	1×10^{17}	9×10^{21}
Shallow uniform donor density N_D (cm^{-3})	1×10^{18}	5×10^{17}	2×10^{18}	1×10^{13}	0
Defect density N_t (cm^{-3})	1×10^{15}	1×10^{15}	1×10^{15}	1×10^{14}	1×10^{14}
References	[52]	[53]	[54]	[55]	[56]

Abbreviations: CB, conduction band; ETL, electron transport layer; FTO, fluorine-doped tin oxide; VB, valence band.

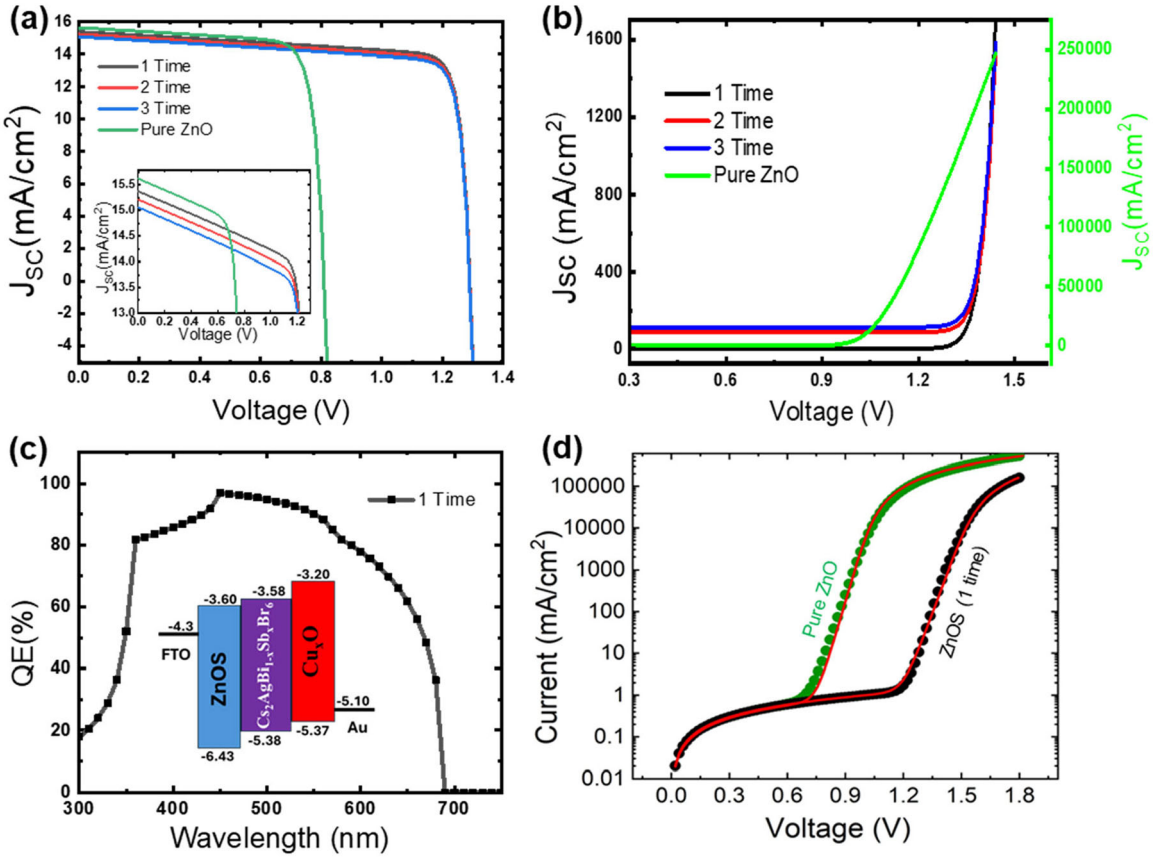

FIGURE 6 | (a, b) Light and dark current *I–V* curve, respectively, (c) the quantum efficiency of one-time coatings, and (d) shows the recombination current curve for one-time coatings.

becomes lower than others. A similar trend observed for the dark current–voltage curve is also shown in Figure 6b.

To understand the variation of the performance parameters better, the semi-log plot of the dark Current-Voltage (IV) of PSCs with undoped and one-time coatings sulfur-doped thin films was investigated, as shown in Figure 6d. The higher dark recombination current (I_o) and series resistance are found for undoped ZnO than ZnOS thin film. This implies that the doped ZnOS exhibits better performance as an ETL layer because of its

TABLE 6 | Optimize PCE using ZnOS experimental data.

Sample	V_{oc} (V)	J_{sc} (mA cm^{-2})	FF (%)	PCE (%)
Pure ZnO	0.8095	15.6207	79.7374	10.0822
1-Time coating	1.2905	15.3729	81.7021	16.2087
2-Times coating	1.2901	15.2133	81.4664	15.9894
3-Times coating	1.2897	15.0601	81.2312	15.7780

Abbreviations: FF, fill factor; PCE, power conversion efficiency.

TABLE 7 | Dark IV parameters for doped and undoped ZnO.

Sample	I_o (mA cm^{-2})	n	R_{sh} (kΩ)	R_s (Ω)
Undoped ZnO	1.03E − 12	1.06	1.06	1.33E − 6
ZnOS (1 time)	9.77E − 16	1.14	1.01	1.16E − 6

low recombination rate, which could enhance the charge carrier mobility of the solar cell. From Section 3 results, it could be predicted that optimum N-doping occurs when the film is annealed for 40 min, resulting in the highest bandgap, which confirms the lowest optical loss, highest hole mobility, and highest carrier concentration that may influence the n and I_o to reduce. The lowest value of I_o leads to the highest device efficiency (Table 7).

Figure 6e shows the external quantum efficiency for the highest-achieved efficiency for the doped ETL prepared by one-time coating in an ambient atmosphere. The inset of Figure 6d shows the band alignment of the proposed device structure, which matches the band with every layer. The best efficiency achieved in this study is 16.21% with a V_{oc} of 1.29 V, a J_{sc} of 15.37 mA cm^{-2}, and an FF of 81.70%. The efficacy of the PSC has been demonstrated to be strongly reliant on the properties of ZnOS thin films, implying that ZnOS ETL needs much more research to achieve the most effective and stable PSC. According to the findings of this study, ZnOS thin film has the potential to be a better ETL than the commonly used ZnO thin film in PSCs.

5 | Conclusion

ZnOS thin films have been fabricated using an unmediated solution process for use as ETL in halide double PSCs. The effects of the number of depositions (increases the thickness due to layer-by-layer deposition) on the surface morphology, structural changes, and optoelectronic characteristics were investigated and compared with undoped ZnO. The ZnOS nanoparticles with three-times coating showed stronger absorption peaks than those of 2 times and 1 time coating may be due to the increase of recrystallization with the increase of thickness as seen in XRD. Consequently, due to the impact of recrystallization, the bandgap energy dropped from 2.76 to 2.68 eV with the increase in the number of depositions. However, the bandgap found for ZnOS is lower than that of ZnO (~3.3 eV) and ZnS (~3.68 eV), suggesting a bandgap bowing effect caused by valence and conduction band shifts. Also, the ZnOS thin film exhibits a large Urbach energy of 292–320 MeV. It shows a high density of band tail states formed within the bandgap, which is decreased with reduced lattice disorder as found in XRD. On the other hand, single deposition film found to be amorphous, whereas 2- and 3-times deposited films observed to be poly-crystalline. The higher crystal growth is found for a higher number of depositions. The FESEM image shows the mesoporous surface of the films. In FTIR, a sharp peak was observed at 422, 428, and 444 cm^{-1}, which can be either due to Zn−S or Zn−O stretching vibrations and validated the formation of ZnOS. In the case of undoped ZnO, the carrier concentration is about 13.08 cm^{-3}, resistivity 8.94×10^{-4} Ω cm, and bandgap 3.2 eV, which is higher than that of ZnOS. However, the mobility of ZnO (10.13 cm^2 V^{-1} s^{-1}) was observed less than that of ZnOS (42.20 cm^2 V^{-1} s^{-1}) thin film, which may influence the device performance. Finally, the SCAPS-1D software has been utilized to analyze and compare the performance between undoped (ZnO) and sulfur-doped (ZnOS) as an ETL in the FTO/ZnOS/$Cs_2AgBi_{0.75}Br_{0.25}Br_6$/$Cu_2O$/Au halide double PSC. Here, we utilized the properties of ETL found in this study, and additional data for other layers have been collected from the literature. For ZnOS ETL, the performance parameter was found to be V_{oc} of 1.29 V, J_{sc} of 15.37 mA cm^{-2}, FF of 81.70%, and PCE of 16.21%. In contrast, the PCE for ZnO thin film is determined to be 10.08% for the identical solar cell device structure. This study gives an indication of the advantages of ZnOS over ZnO for halide double PSCs. The findings may help construct a high-efficiency halide double perovskite in the future.

Author Contributions

Md. Jakir Hossen: conceptualization, data curation, formal analysis, methodology, visualization, writing – original draft, writing – review and editing. **Md. Bulu Rahman:** formal analysis, software, writing – review and editing. **M. Shahinuzzaman:** resources, validation, visualization, writing – review and editing. **Md. Helal Miah:** data curation, investigation, visualization, writing – review and editing. **Noor-E. Ashrafi:** software, writing – review and editing. **Abdur Rahim:** methodology, resources, visualization, writing – review and editing. **Suhana Mohd. Said:** funding acquisition, investigation, supervision, validation. **S. F. W. M. Hatta:** investigation, project administration, resources, supervision, validation. **Mohammad Aminul Islam:** conceptualization, funding acquisition, investigation, project administration, supervision, validation, writing – review and editing.

Acknowledgments

This study was supported by the Malaysian Ministry of Higher Education through FRGS grant FRGS/1/2020/TK0/UM/02/33 and Malayasian Internal Scholarship 2022. The authors also acknowledge the support from the Faculty of Engineering, Universiti Malaya (@UM).

Conflicts of Interest

The authors declare no conflicts of interest.

Data Availability Statement

All data are available in the Manuscript. All the data presented in the manuscript will be available upon request to the corresponding author.

References

1. National Renewable Energy Laboratory, *NREL Best Research-Cell PV Efficiency Chart* (2025).

2. R. Runjhun, E. A. Alharbi, Z. Drużyński, et al., "High-Performance Perovskite Solar Cells With Zwitterion-Capped-ZnO Quantum Dots as Electron Transport Layer and NH4X (X = F, Cl, Br) Assisted Interfacial Engineering," *Energy and Environmental Materials* 7, no. 5 (2024): e12720, https://doi.org/10.1002/eem2.12720.

3. N. A. Zainal Abidin, F. Arith, N. S. Noorasid, et al., "Dopant Engineering for ZnO Electron Transport Layer Towards Efficient Perovskite Solar Cells," *RSC Advances* 13, no. 48 (2023): 33797–33819, https://doi.org/10.1039/d3ra04823c.

4. R. D. Chavan, M. Wolska-Pietkiewicz, D. Prochowicz, et al., "Organic Ligand-Free ZnO Quantum Dots for Efficient and Stable Perovskite Solar Cells," *Advanced Functional Materials* 32 (2022): 2205909, https://doi.org/10.1002/adfm.202205909.

5. H. Si, X. Zhao, Z. Zhang, Q. Liao, and Y. Zhang, "Low-Temperature Electron-Transporting Materials for Perovskite Solar Cells: Fundamentals, Progress, and Outlook," *Coordination Chemistry Reviews* 500 (2024): 215502, https://doi.org/10.1016/j.ccr.2023.215502.

6. B. T. Liu, B. W. Guo, and R. Balamurugan, "Effect of Polyethylene Glycol Incorporation in Electron Transport Layer on Photovoltaic Properties of Perovskite Solar Cells," *Nanomaterials* 10, no. 9 (2020): 1753, https://doi.org/10.3390/nano10091753.

7. S. Zahid, S. Ali, Y. Jamil, and J. Iqbal, "Computational Screening of 3,5-Dicarbonitrilepyridine (DCP) Core Based Eco-Friendly Solvent Processed Hole-Transport Materials for Perovskite Solar Cells: A DFT and TD-DFT Study," *Journal of Physics and Chemistry of Solids* 207 (2025): 112866, https://doi.org/10.1016/j.jpcs.2025.112866.

8. S. Panigrahi, S. K. Mukaddar, S. Jana, et al., "Tailoring the Interface in High Performance Planar Perovskite Solar Cell by ZnOS Thin Film," *ACS Applied Energy Materials* 5, no. 5 (2022): 5680–5690, https://doi.org/10.1021/acsaem.1c04064.

9. H. Zhou, Q. Chen, G. Li, et al., "Interface Engineering of Highly Efficient Perovskite Solar Cells," *Science* 345, no. 6196 (2014): 542–546, https://doi.org/10.1126/science.125405.

10. O. K. Echendu, S. Z. Werta, F. B. Dejene, and V. Craciun, "Electrochemical Deposition and Characterization of ZnOS Thin Films for Photovoltaic and Photocatalysis Applications," *Journal of Alloys and Compounds* 769 (2018): 201–209, https://doi.org/10.1016/j.jallcom.2018.07.327.

11. R. L. Garris, J. V. Li, M. A. Contreras, et al., "Efficient and Stable CIGS Solar Cells With ZnOS Buffer Layer," in *2014 IEEE 40th Photovoltaic Specialist Conference, PVSC 2014* (2014), 353–356, https://doi.org/10.1109/PVSC.2014.6924930.

12. S. Y. Yu, M. A. Hassan, M. A. Johar, and S. W. Ryu, "Optical and Structural Analysis of Zinc Oxysulfide Digital Alloys Grown by Atomic Layer Deposition," *Journal of the Korean Physical Society* 73, no. 5 (2018): 649–655, https://doi.org/10.3938/jkps.73.649.

13. D.-S. Lee and H.-D. Jeong, "Distinct Band Gap Tunability of Zinc Oxysulfide (ZnOS) Thin Films Synthesized From Thioacetate-Capped ZnO Nanocrystals," *Applied Science and Convergence Technology* 23, no. 6 (2014): 376–386, https://doi.org/10.5757/asct.2014.23.6.376.

14. X. F. Fan, Z. X. Shen, Y. M. Lu, and J. L. Kuo, "A Theoretical Study of Thermal Stability and Electronic Properties of Wurtzite and Zinc-blende ZnO_xS_{1-x}," *New Journal of Physics* 11 (2009): 093008, https://doi.org/10.1088/1367-2630/11/9/093008.

15. D. Dwivedi, T. A. Patel, and E. Panda, "Simple, Inexpensive Way of Fabricating High Quality Zn(O)S Nanoparticles by Varying pH," *Materials Science in Semiconductor Processing* 79 (2018): 1–6, https://doi.org/10.1016/j.mssp.2018.01.016.

16. A. Grimm, D. Kieven, R. Klenk, et al., "Junction Formation in Chalcopyrite Solar Cells by Sputtered Wide Gap Compound Semiconductors," *Thin Solid Films* 520, no. 4 (2011): 1330–1333, https://doi.org/10.1016/j.tsf.2011.04.150.

17. W. J. Choi, W. W. Park, Y. Kim, C. S. Son, and D. Hwang, "The Effect of AlD-Zn(O,S) Buffer Layer on the Performance of CIGSSe Thin Film Solar Cells," *Energies* 13, no. 2 (2020): 412, https://doi.org/10.3390/en13020412.

18. A. Z. Arsad, N. A. Arzaee, S. F. Abdullah, et al., "Effects of Post-Deposition Treatment on Zinc Sulfide Thin Films Prepared by an Effective-Cost Chemical Bath Deposition Method," *Ceramics International* 50, no. 11 (2024): 18697–18707, https://doi.org/10.1016/j.ceramint.2024.02.358.

19. A. Lakshmanan, Z. C. Alex, and S. R. Meher, "Experimental and Ab Initio Studies of the Structural and Optoelectronic Properties of Hexagonal Wurtzite $ZnO_{1-x}S_x$ Alloys," *Materials Chemistry and Physics* 312 (2024): 128674, https://doi.org/10.1016/j.matchemphys.2023.128674.

20. B. K. Meyer, A. Polity, B. Farangis, et al., "On the Composition Dependence of $ZnO_{1-x}S_x$," *Physica Status Solidi (C)* 1, no. 4 (2004): 694–697, https://doi.org/10.1002/pssc.200304256.

21. V. A. Elyukhin, "Spinodal Decomposition Ranges of Wurtzite and Zinc Blende ZnB VI_xO_{1-x} (BVI=S, Se, Te) Alloys," *Journal of Crystal Growth* 380 (2013): 153–156, https://doi.org/10.1016/j.jcrysgro.2013.06.007.

22. K. Dileep, R. Sahu, K. K. Nagaraja, and R. Datta, "Crystallographic Phase Separation and Band Gap of $ZnO_{1-x}S_x$ (x=0.1–0.3) Alloy Thin Films Grown by Pulsed Laser Deposition," *Journal of Crystal Growth* 402 (2014): 124–129, https://doi.org/10.1016/j.jcrysgro.2014.05.017.

23. I. Shtepliuk, V. Khomyak, V. Khranovskyy, and R. Yakimova, "Valence Band Structure and Optical Properties of $ZnO_{1-x}S_x$ Ternary Alloys," *Journal of Alloys and Compounds* 649 (2015): 878–884, https://doi.org/10.1016/j.jallcom.2015.07.143.

24. T. Islam, R. Jani, S. Amin, et al., "Simulation Studies to Quantify the Impacts of Point Defects: An Investigation of $Cs_2AgBiBr_6$ Perovskite Solar Devices Utilizing ZnO and Cu_2O as the Charge Transport Layers," *Computational Materials Science* 184, no. 184 (2020): 109865, https://doi.org/10.1016/j.commatsci.2020.109865.

25. M. Jakir Hossen, H. M. Hamzah, M. Shahinuzzaman, et al., "Recent Progress on the Efficiency and Stability of Lead-Free $Cs_2AgBiBr_6$ Double Halide Perovskite Solar Cells," *Physica Scripta* 100 (2025): 012005, https://doi.org/10.1088/1402-4896/ad9b59.

26. Y. Liu, L. Zhang, M. Wang, et al., "Bandgap-Tunable Double-Perovskite Thin Films by Solution Processing," *Materials Today* 28, no. September (2019): 25–30, https://doi.org/10.1016/j.mattod.2019.04.023.

27. A. Kumar, S. K. Swami, S. S. Rawat, V. N. Singh, O. P. Sinha, and R. Srivastava, "Mixed Bismuth-Antimony-Based Double Perovskite Nanocrystals for Solar Cell Application," *International Journal of Energy Research* 45, no. 11 (2021): 16769–16780, https://doi.org/10.1002/er.6924.

28. K. S. Hwang, T. Manabe, T. Nagahama, I. Yamaguchi, T. Kumagai, and S. Mizuta, "Effect of Substrate Material on the Crystallinity and Epitaxy of $Pb(Zr,Ti)O_3$ Thin Films," *Thin Solid Films* 347, no. 1–2 (1999): 106–111, https://doi.org/10.1016/s0040-6090(98)01727-1.

29. A. Hannan, M. S. Islam, S. R. Parvin, and M. J. Hossen, "Unusual Crystal-Lattice Behaviour of CeSb at Ambient Pressure," *Journal of the National Science Foundation of Sri Lanka* 38, no. 3 (2010): 201–205, https://doi.org/10.4038/jnsfsr.v38i3.2310.

30. J. C. Tauce, *Optical Properties of Solids* (Academic Press, 1972).

31. Y. Shi, D. S. Kim, T. Kim, H. Ahn, and I. Bin, "Structural, Electrical and Optical Properties of In-Doped CdS Thin Films Prepared by Vacuum Coevaporation," *Thin Solid Films* 229, no. 2 (1993): 227–231.

32. F. Urbach, "The Long-Wavelength Edge of Photographic," *Physical Review* 92 (1953): 1324, https://doi.org/10.1103/PhysRev.92.1324.

33. R. Bhatt, I. Bhaumik, S. Ganesamoorthy, et al., "Urbach Tail and Bandgap Analysis in Near Stoichiometric Linbo 3 Crystals," *Physica Status Solidi (A)* 209, no. 1 (2012): 176–180, https://doi.org/10.1002/pssa.201127361.

34. M. A. Islam, M. S. Hossain, M. M. Aliyu, et al., "Comparison of Structural and Optical Properties of CdS Thin Films Grown by CSVT, CBD and Sputtering Techniques," *Energy Procedia* (2013): 203–213, https://doi.org/10.1016/j.egypro.2013.05.059.

35. R. Singh and R. Raj Singh, "Unmediated One-Step Synthesis of Novel ZnSO for Photovoltaic and Electronic Applications," *Materials Letters* 324 (2022): 132651, https://doi.org/10.1016/j.matlet.2022.132651.

36. S. Chandra Tudu, M. Zubko, J. Kusz, and A. Bhattacharjee, *Structural, Morphological and Optical Characterization of Green Synthesized ZnS Nanoparticles Using* Azadirachta indica *(Neem) Leaf Extract* (2020).

37. E. Keleş Güner, R. Akkaş, and A. Özer, "Synthesis of Zinc Sulfate Hydroxide Trihydrate by Chemical Precipitation and Its Transformation to Zinc Oxide," *Chemical Engineering Communications* 209, no. 9 (2022): 1203–1213, https://doi.org/10.1080/00986445.2021.1953486.

38. K. R. Naveenkumar, P. Kannappan, K. Asokan, et al., "Studies on Structural and Optical Characterization of Na:ZnS Nanocomposites," *Physica Scripta* 98, no. 7 (2023): 075948, https://doi.org/10.1088/1402-4896/acdda7.

39. W. Ahmed, E. L. Osborne, A. V. Veluthandath, and G. Senthil Murugan, "A Rapid and Simplified Approach to Correct Atmospheric Absorptions in Infrared Spectra," *Analytical Chemistry* 96, no. 45 (2024): 18052–18060, https://doi.org/10.1021/acs.analchem.4c03594.

40. J. Singh, R. Heinz, and R. Chen, *Impact of Active Gas Purge on FTIR Measurements Technical Note* (Thermo Scientific, 2025).

41. X. Zhang, G. Wu, Z. Gu, et al., "Active-Layer Evolution and Efficiency Improvement of $(CH_3NH_3)Bi_2I_9$-based Solar Cell on TiO_2-deposited ITO Substrate," *Nano Research* 9, no. 10 (2016): 2921–2930, https://doi.org/10.1007/s12274-016-1177-8.

42. K. Domanski, E. A. Alharbi, A. Hagfeldt, M. Grätzel, and W. Tress, "Systematic Investigation of the Impact of Operation Conditions on the Degradation Behaviour of Perovskite Solar Cells," *Nature Energy* 3, no. 1 (2018): 61–67, https://doi.org/10.1038/s41560-017-0060-5.

43. S. Seo, S. Jeong, C. Bae, N. G. Park, and H. Shin, "Perovskite Solar Cells With Inorganic Electron- and Hole-Transport Layers Exhibiting Long-Term (≈500 h) Stability at 85°C under Continuous 1 Sun Illumination in Ambient Air," *Advanced Materials* 30, no. 29 (2018): 1801010, https://doi.org/10.1002/adma.201801010.

44. H. Tan, A. Jain, O. Voznyy, et al., "Efficient and Stable Solution-Processed Planar Perovskite Solar Cells via Contact Passivation," *Science* 355, no. 6326 (2017): 722–726, https://doi.org/10.1126/science.aai9081.

45. N. Olejnik-Fehér, M. Jędrzejewska, M. Wolska-Pietkiewicz, D. Lee, G. D. Paëpe, and J. Lewiński, "On the Fate of Lithium Ions in Sol–Gel Derived Zinc Oxide Nanocrystals," *Small* 20, no. 28 (2024): 1–9, https://doi.org/10.1002/smll.202309984.

46. M. Burgelman, K. Decock, A. Niemegeers, J. Verschraegen, and S. Degrave, *SCAPS Gent Manual* (University of Gent, 2025).

47. F. Liu, J. Zhu, J. Wei, et al., "Numerical Simulation: Toward the Design of High-Efficiency Planar Perovskite Solar Cells," *Applied Physics Letters* 104, no. 25 (2014): 253508, https://doi.org/10.1063/1.4885367.

48. S. Zandi, P. Saxena, M. Razaghi, and N. E. Gorji, "Simulation of CZTSSe Thin-Film Solar Cells in COMSOL: Three-Dimensional Optical, Electrical, and Thermal Models," *IEEE Journal of Photovoltaics* 10, no. 5 (2020): 1503–1507, https://doi.org/10.1109/JPHOTOV.2020.2999881.

49. M. Kumar, A. Kumar, A. Raj, P. C. Sati, M. Sahni, and A. Anshul, "Organic–Inorganic Perovskite-Based Solar Cell Designs for High Conversion Efficiency: A Comparative Study by SCAPS Simulation," *Materials Today: Proceedings* 49, no. 8 (2020): 3081–3087, https://doi.org/10.1016/j.matpr.2020.11.035.

50. N. Rai and D. K. Dwivedi, "Numerical Modelling for Enhancement of Output Performance of CIGS Based Thin Film Solar Cell Using SCAPS 1-D Simulation Software," in *AIP Conference Proceedings* (American Institute of Physics Inc., 2020), https://doi.org/10.1063/5.0001233.

51. M. J. Hossen, M. B. Rahman, M. H. Miah, et al., "Modeling and Optimization of High Efficiency Pb-Free Cs-Based Halide Double Perovskite Solar Cell Using SCAPS-1D," *Journal of Optics* (2025): s12596-025-02550-9, https://doi.org/10.1007/s12596-025-02550-9.

52. U. Mandadapu, "Simulation and Analysis of Lead Based Perovskite Solar Cell Using SCAPS-1D," *Indian Journal of Science and Technology* 10, no. 1 (2017): 1–8, https://doi.org/10.17485/ijst/2017/v11i10/110721.

53. D. Jalalian, A. Ghadimi, and A. Kiani, "Modeling of a High Performance Bandgap Graded Pb-Free HTM-Free Perovskite Solar Cell," *European Physical Journal Applied Physics* 87, no. 1 (2019): 10101, https://doi.org/10.1051/epjap/2019190095.

54. S. I. Rahman, S. Faisal, S. Ahmed, and T. I. Dhrubo, "A Comparative Study on Different HTMs in Perovskite Solar Cell With ZnOS Electron Transport Layer," in *5th IEEE Region 10 Humanitarian Technology Conference 2017, R10-HTC 2017* (Institute of Electrical and Electronics Engineers Inc., 2018), 546–550, https://doi.org/10.1109/R10-HTC.2017.8289019.

55. J. Madan, Shivani, R. Pandey, and R. Sharma, "Device Simulation of 17.3% Efficient Lead-Free All-Perovskite Tandem Solar Cell," *Solar Energy* 197 (2020): 212–221, https://doi.org/10.1016/j.solener.2020.01.006.

56. M. I. Hossain, F. H. Alharbi, and N. Tabet, "Copper Oxide as Inorganic Hole Transport Material for Lead Halide Perovskite Based Solar Cells," *Solar Energy* 120 (2015): 370–380, https://doi.org/10.1016/j.solener.2015.07.040.

57. Y. Shao, Y. Yuan, and J. Huang, "Correlation of Energy Disorder and Open-Circuit Voltage in Hybrid Perovskite Solar Cells," *Nature Energy* 1, no. 1 (2016): 15001, https://doi.org/10.1038/nenergy.2015.1.

58. E. Edri, S. Kirmayer, A. Henning, et al., "Why Lead Methylammonium Tri-Iodide Perovskite-Based Solar Cells Require a Mesoporous Electron Transporting Scaffold (But Not Necessarily a Hole Conductor)," *Nano Letters* 14, no. 2 (2014): 1000–1004, https://doi.org/10.1021/nl404454h.